Investigation of the impact of zeolite shaping and salt deposition on the characteristics and performance of composite thermochemical heat storage systems.

-Supplementary data-

Quentin Touloumet[a], Georgeta Postole[a*], Laurence Massin[a], Chantal Lorentz[a], Aline Auroux[a*]

[a] *Univ Lyon, Université Claude Bernard Lyon 1, CNRS, IRCELYON, F-69626 Villeurbanne, France*

Corresponding authors: georgeta.postole@ircelyon.univ-lyon1.fr
aline.auroux@ircelyon.univ-lyon1.fr

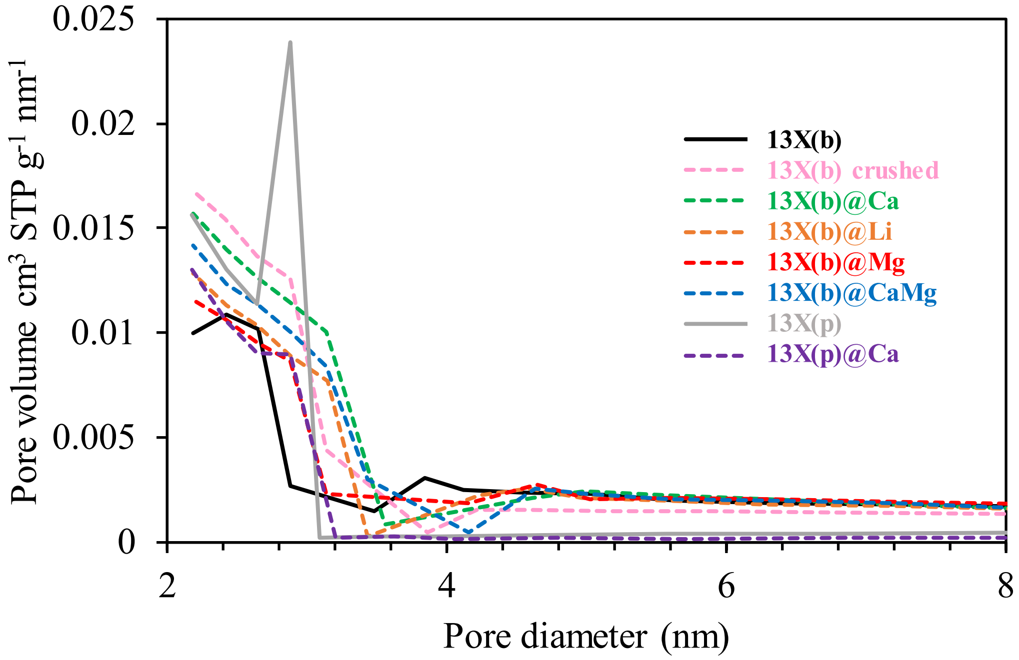

Figure S1. Pore size distribution of 13X based materials between 2-8 nm.

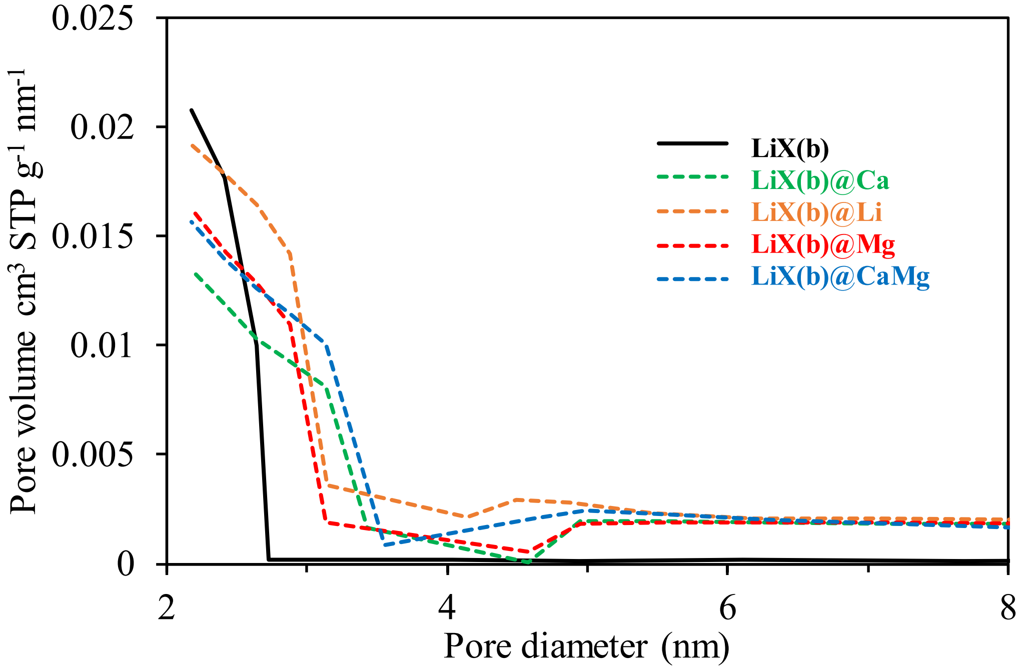

Figure S2. Pore size distribution of LiX(b) and corresponding composites between 2-8 nm.

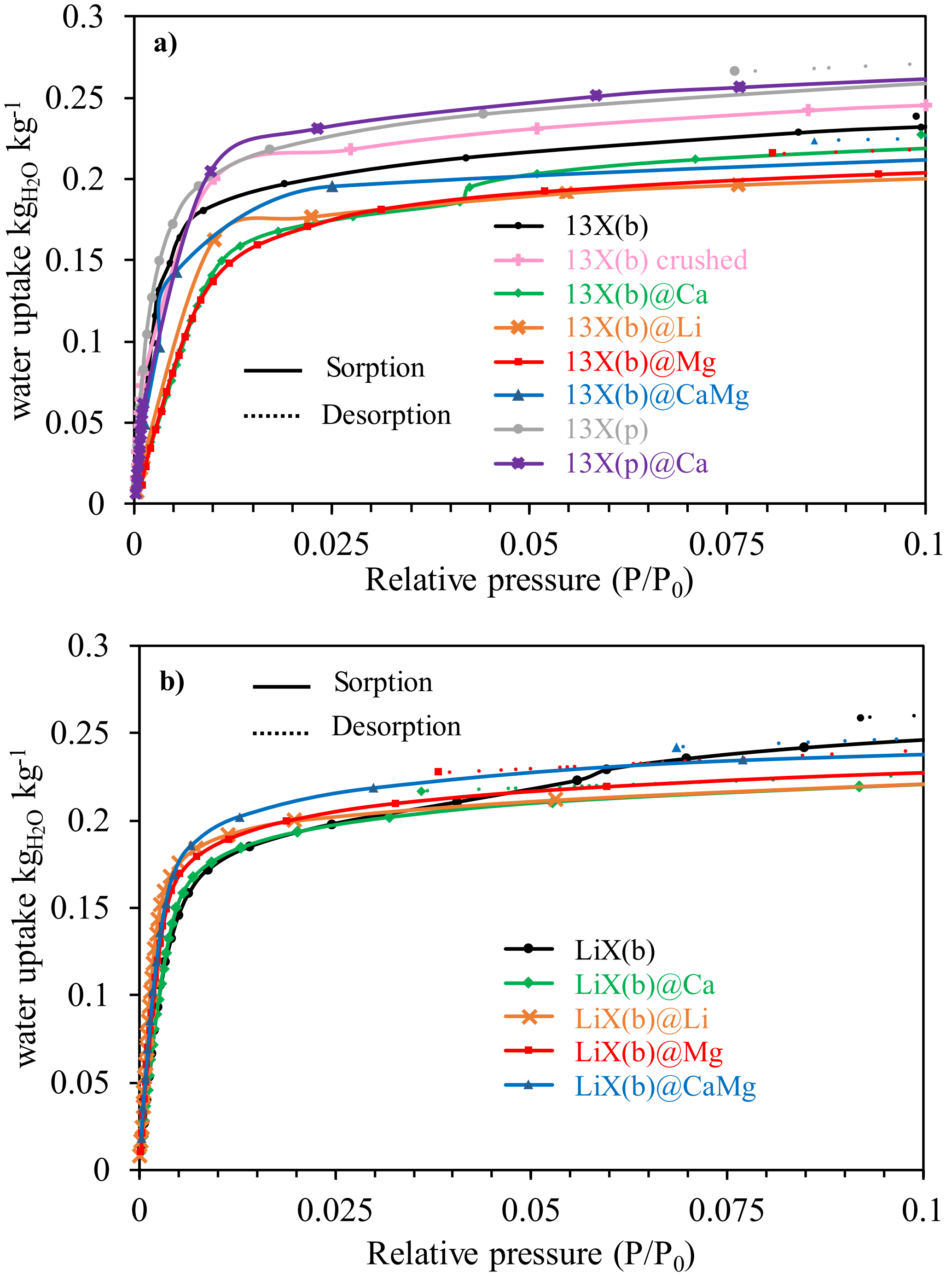

Figure S3. Water vapor sorption/desorption isotherms at 25 °C of 13X (a) and LiX (b) and corresponding composites.

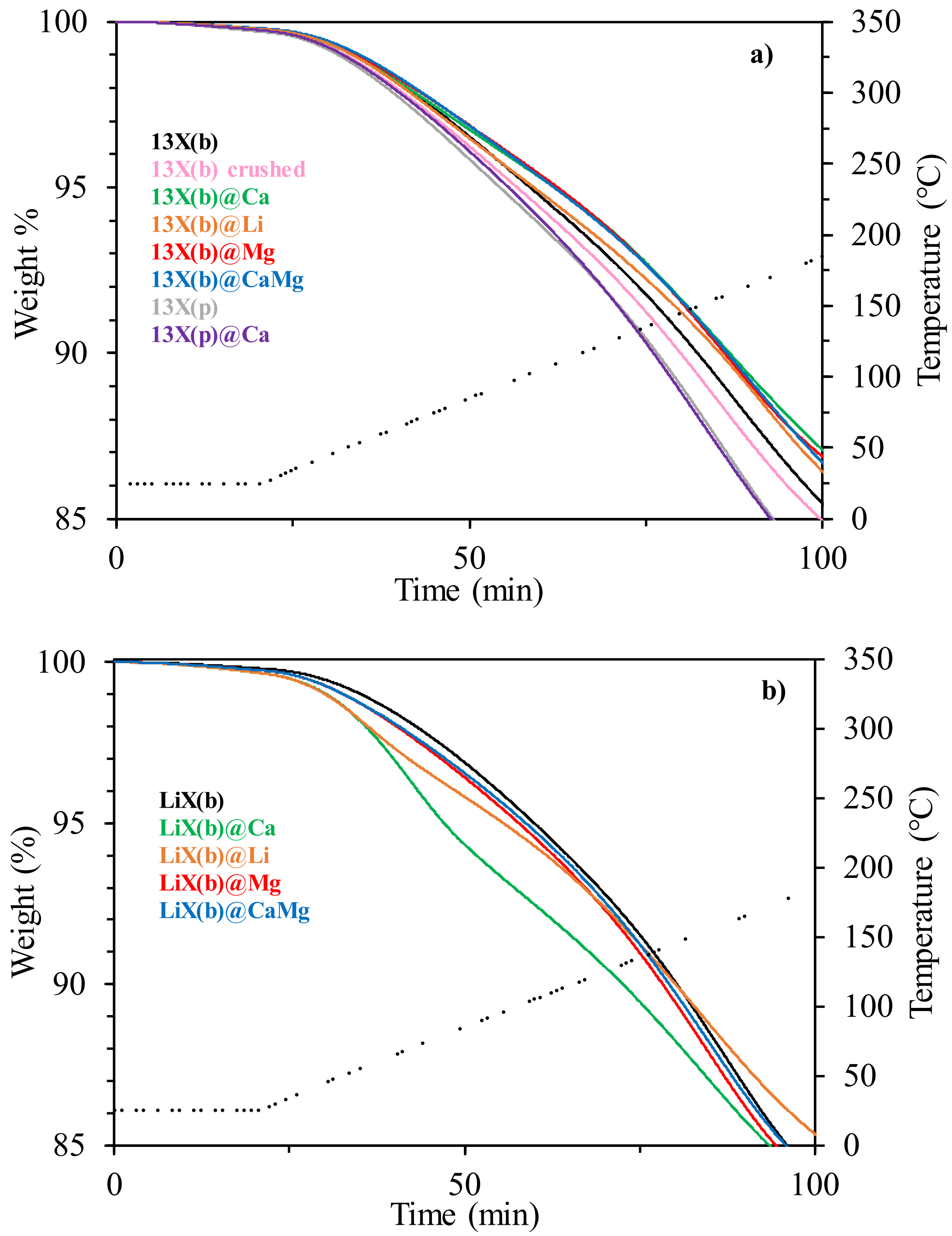

Figure S4. Weight evolution during first 100 min of the second dehydration of 13X (a) and LiX (b) and corresponding composites

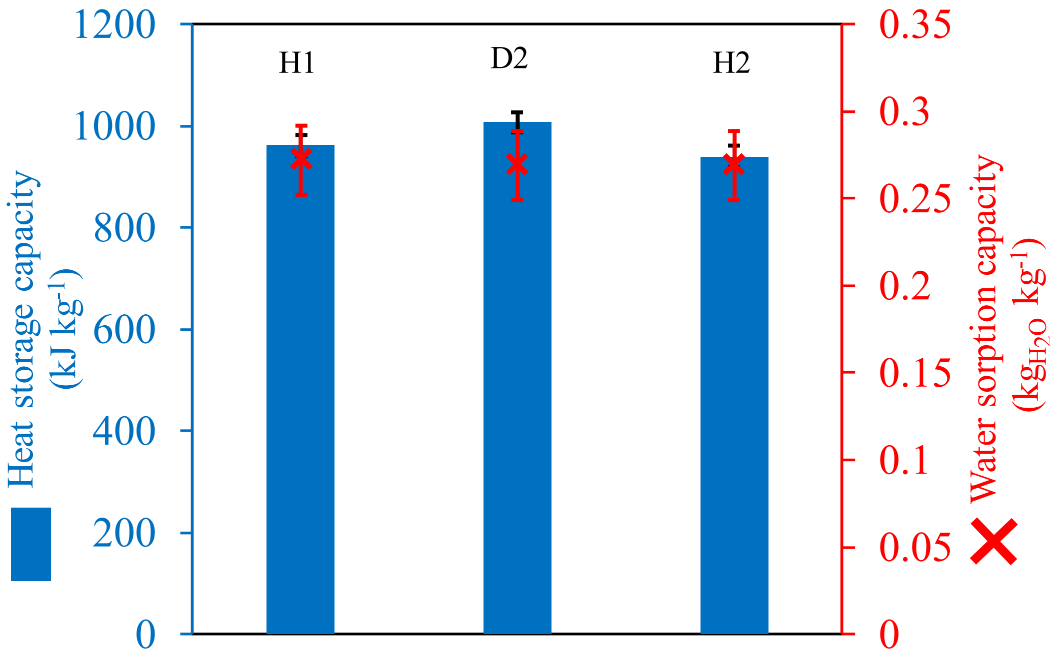

Figure S5. Heat and water storage capacities of 13X(b) during first hydration (H1), second dehydration (D2) and second hydration (H2).

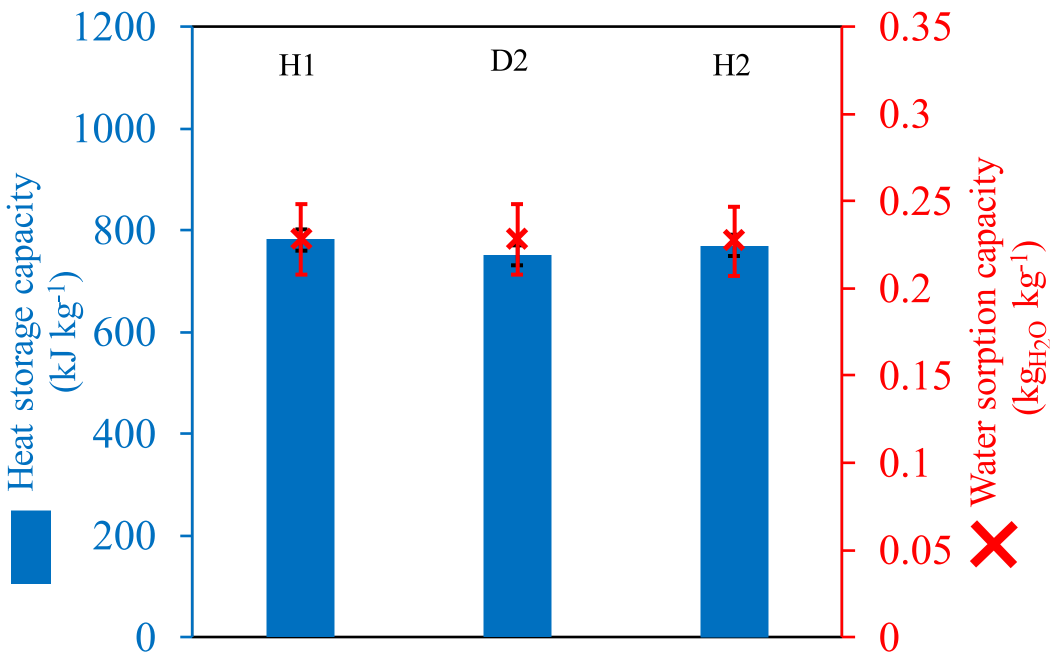

Figure S6. Heat and water storage capacities of 13X(b)@Ca during first hydration (H1), second dehydration (D2) and second hydration (H2).

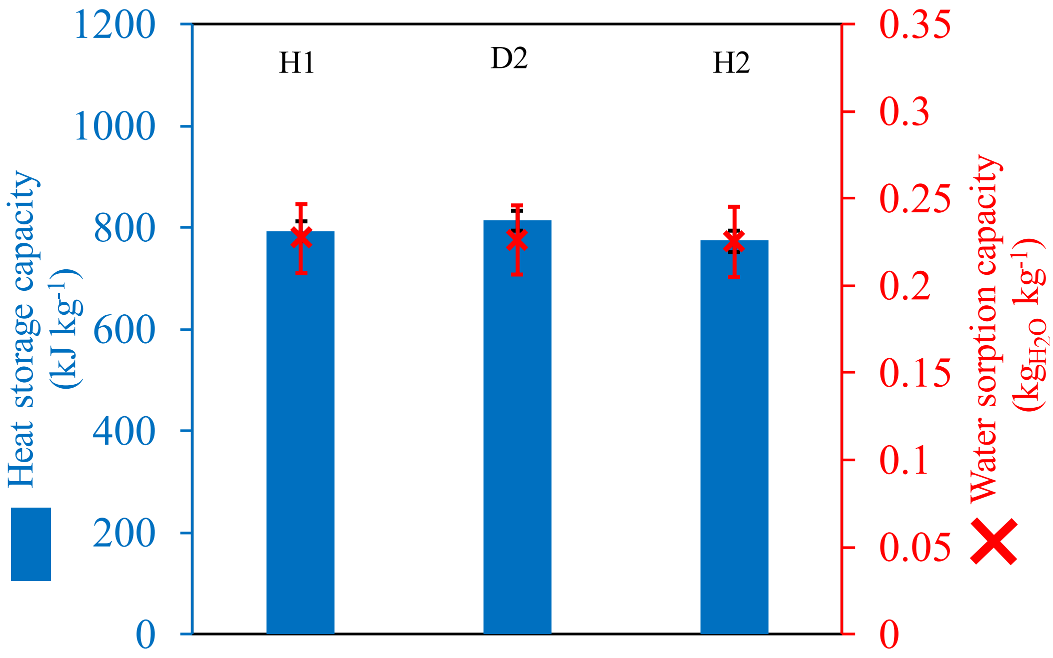

Figure S7. Heat and water storage capacities of 13X(b)@Mg during first hydration (H1), second dehydration (D2) and second hydration (H2).

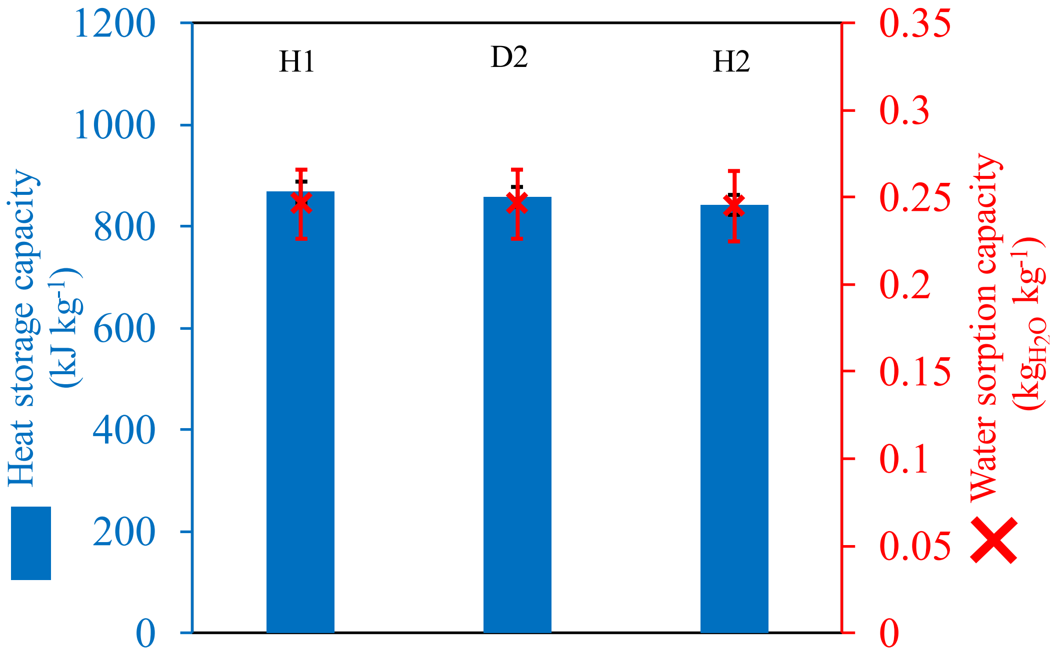

Figure S8. Heat and water storage capacities of 13X(b)@Li during first hydration (H1), second dehydration (D2) and second hydration (H2).

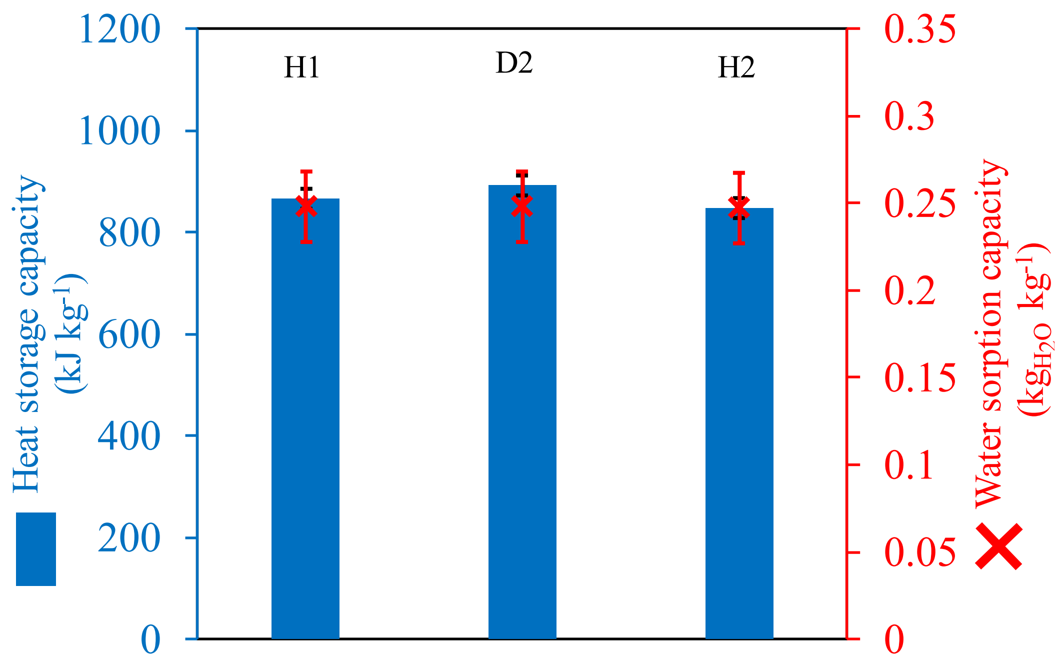

Figure S9. Heat and water storage capacities of 13X(b)@CaMg during first hydration (H1), second dehydration (D2) and second hydration (H2).

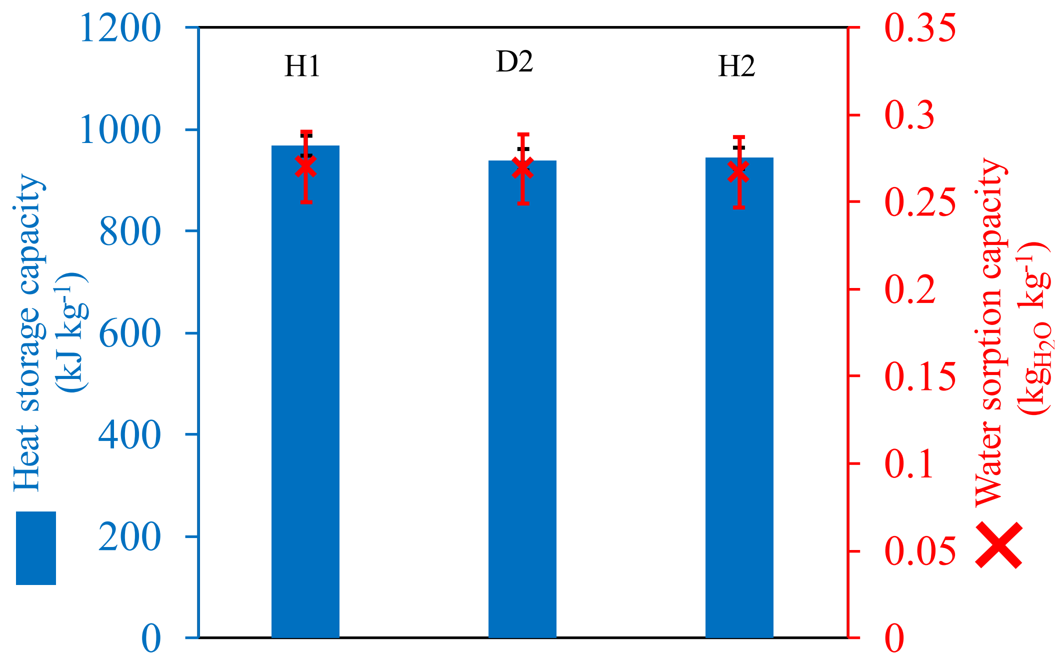

Figure S10. Heat and water storage capacities of 13X(b) crushed during first hydration (H1), second dehydration (D2) and second hydration (H2).

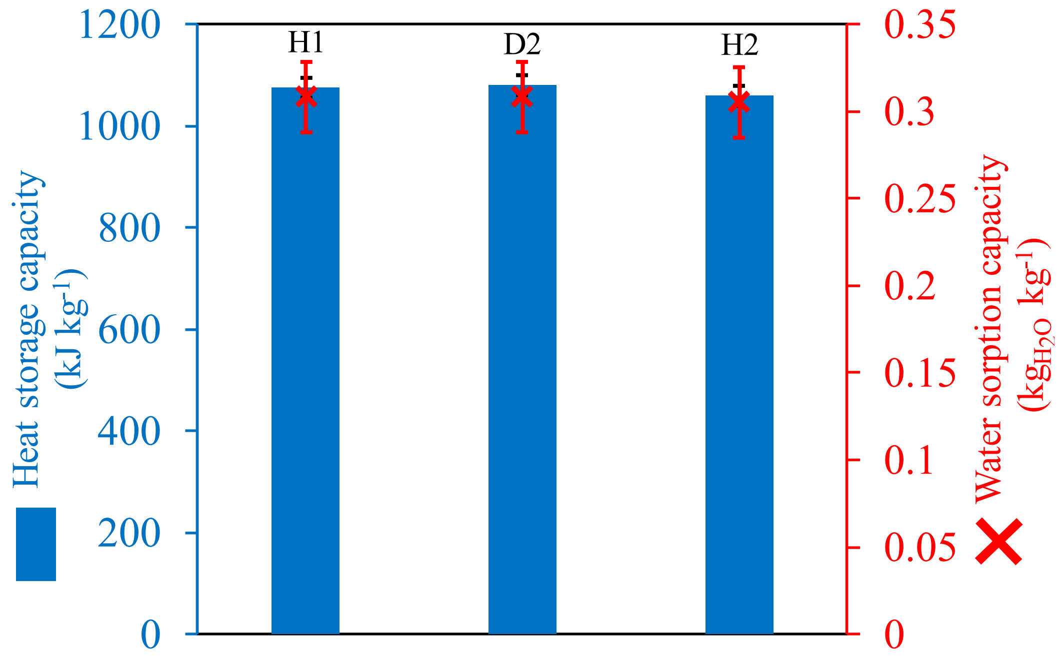

Figure S11. Heat and water storage capacities of 13X(p) during first hydration (H1), second dehydration (D2) and second hydration (H2).

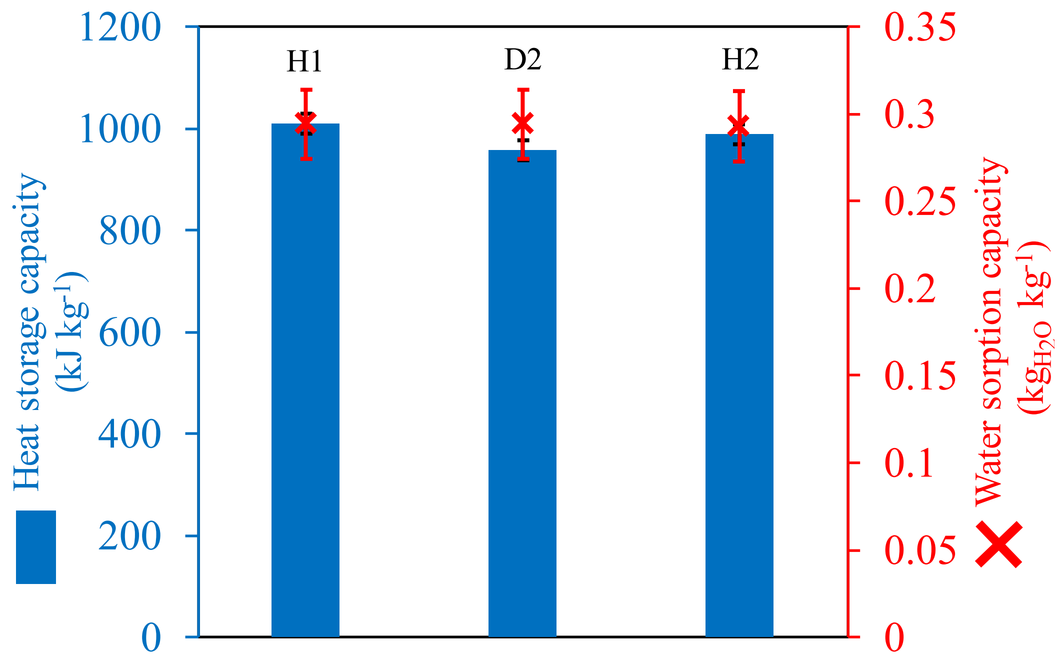

Figure S12. Heat and water storage capacities of 13X(p)@Ca during first hydration (H1), second dehydration (D2) and second hydration (H2).

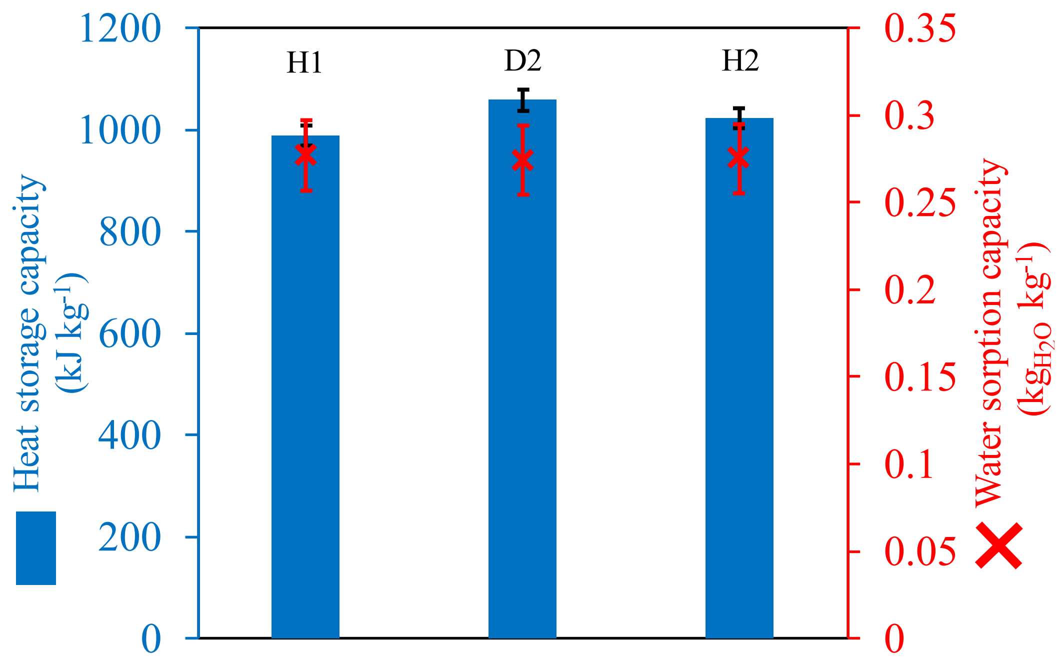

Figure S13. Heat and water storage capacities of LiX(b) during first hydration (H1), second dehydration (D2) and second hydration (H2).

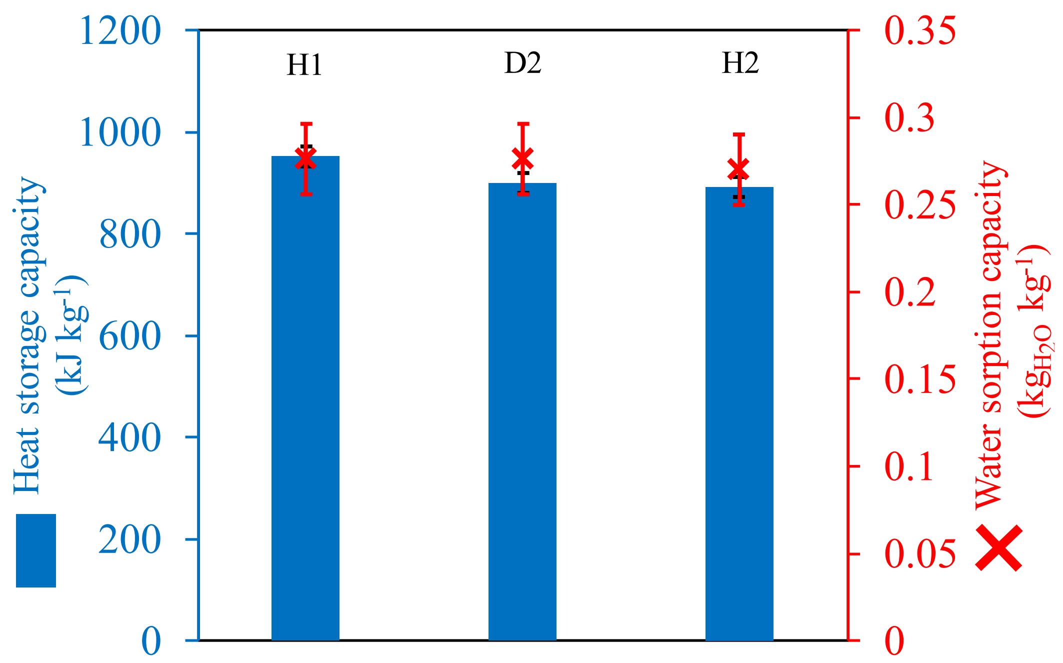

Figure S14. Heat and water storage capacities of LiX(b)@Ca during first hydration (H1), second dehydration (D2) and second hydration (H2).

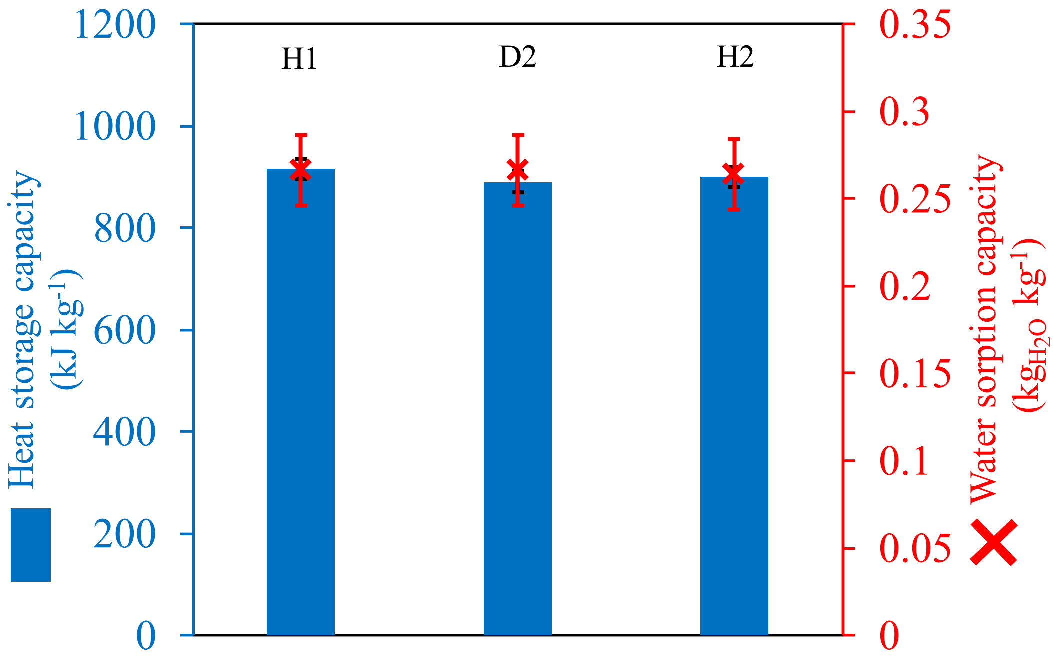

Figure S15. Heat and water storage capacities of LiX(b)@Mg during first hydration (H1), second dehydration (D2) and second hydration (H2).

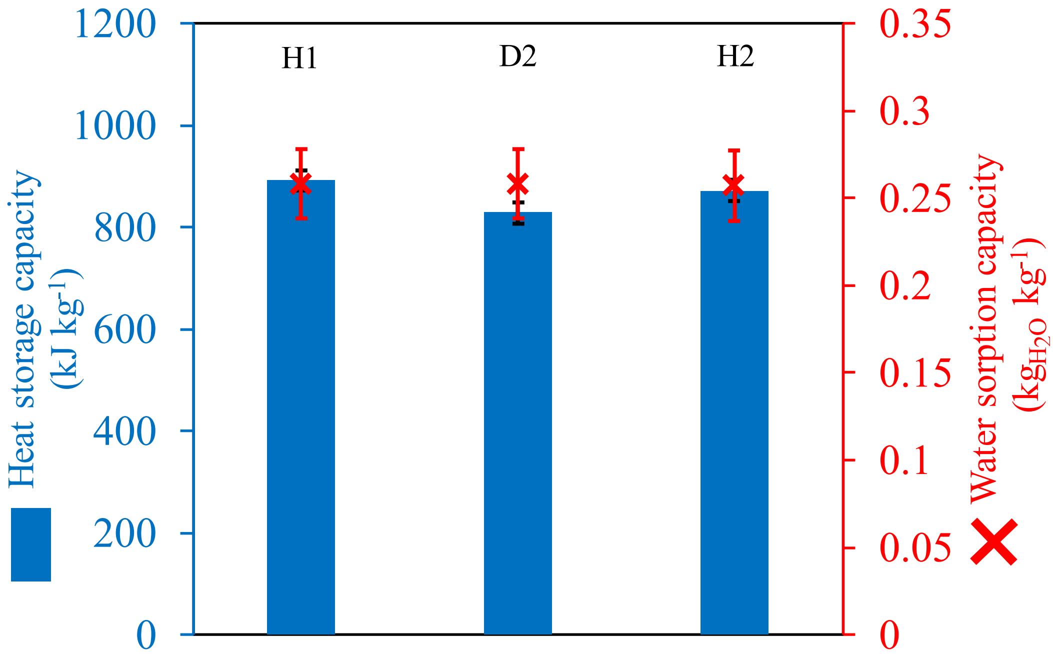

Figure S16. Heat and water storage capacities of LiX(b)@Li during first hydration (H1), second dehydration (D2) and second hydration (H2).

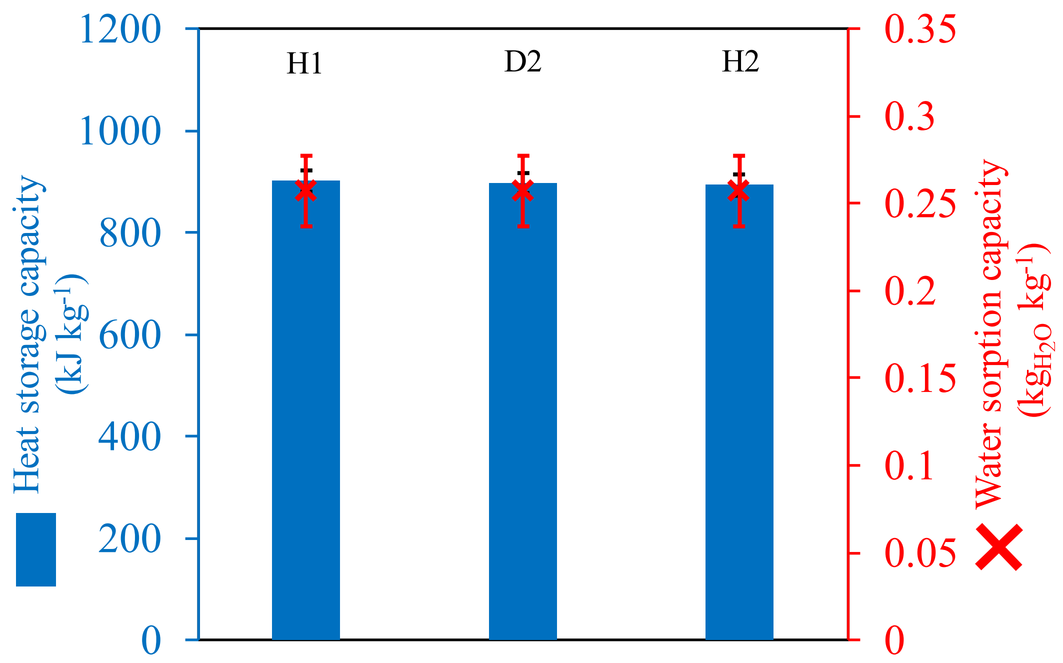

Figure S17. Heat and water storage capacities of LiX(b)@CaMg during first hydration (H1), second dehydration (D2) and second hydration (H2).

Table S1. Comparison of storage performances between studied composites-based zeolites and other composites in literature.

Host matrix	Salt content (wt.%)[a]	Hydration temperature (°C)	RH during hydration (%)	Dehydration temperature (°C)	Water sorption capacity (kg_{H_2O} kg^{-1})[b]	Heat storage capacity (kJ kg^{-1})[c]	Ref.
Host matrices							
13X(b)	-	25	30	300	0.28	1007	This work
13X(p)	-	25	30	300	0.28	1080	This work
LiX(b)	-	25	30	300	0.28	1058	This work
13X	-	20	55	150	-	928	[1]
NaY	-	20	55	150	-	978	[1]
SBA-15	-	20	30	150	0.04	-	[2]
MCM-41	-	20	30	150	0.04	-	[2]
AlPO-5	-	r.t.	30	400	0.237	703	[3]
AlPO-18	-	r.t.	30	400	0.283	1192	[3]
Composites							
13X(b)	4.8 wt% $CaCl_2$	25	30	300	0.29	**0.21**	This work
13X(b)	4.8 wt% $MgSO_4$	25	30	300	0.26	**0.17**	This work
13X(b)	5.1 wt% of LiCl	25	30	300	0.28	**0.19**	This work
13X(b)	2.6 wt% $CaCl_2$ + 2.5 wt% $MgSO_4$	25	30	300	0.28	**0.20**	This work
13X(p)	4.6 wt% $CaCl_2$	25	30	300	0.29	972	This work
LiX(b)	5.2 wt% $CaCl_2$	25	30	300	0.28	900	This work
LiX(b)	5.4 wt% $MgSO_4$	25	30	300	0.28	890	This work
LiX(b)	4.7 wt% of LiCl	25	30	300	0.26	892	This work
LiX(b)	2.7 wt% $CaCl_2$ + 2.5 wt% $MgSO_4$	25	30	300	0.26	897	This work
SBA-15	7 wt% $Al_2(SO_4)_3$	20	30	150	0.17	612	[2]
MCM-41	7 wt% $Al_2(SO_4)_3$	20	30	150	0.09	334	[2]
13X	15 wt% $MgSO_4$	30	60	300	0.205	636	[4]
13X	10.8 wt% $MgSO_4$	25	80	150	-	632	[5]
Silica gel	13.8 wt% $CaCl_2$	20	30	300	0.23	746	[6]
Alumina	14.4 wt% $CaCl_2$	20	30	300	0.17	576	[6]
Mesoporous ordered silica	4 wt% $CaCl_2$	40	16.6	120	0.10	292	[7]

Mesoporous ordered silica	4 wt% $CaCl_2$	40	16.6	120	0.14	428	[7]
MIL-100(Fe)	46 wt% $CaCl_2$	30	86	80	0.47	1206	[8]
MIL-101(Cr)	62 wt% $CaCl_2$	30	86	80	0.58	1728	[8]
SBA-15	62 wt% $CaCl_2$	25	30	150	-	1698	[9]

[a] Determined by ICP-OES (±2%).[b] Water sorption capacity determined with Eq. (2) on dehydrated sample at 300 °C (± 0.02). [c] Dehydration heat determined by 2nd dehydration heat flow integration (± 20 kJ kg^{-1}).

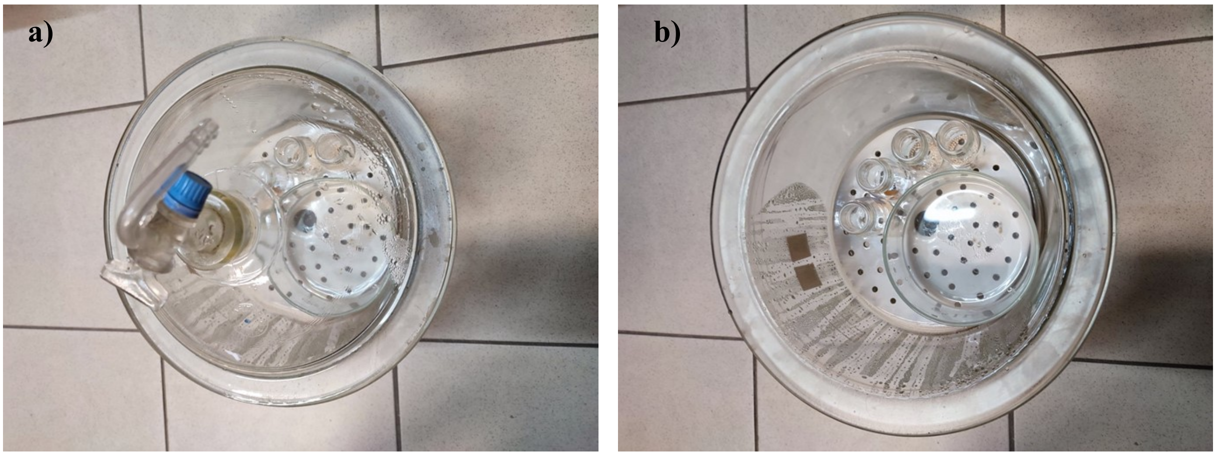

Figure S18. Photography of the water satured environment with studied materials closed (a) and open (b).

Table S2. Textural characterization of materials after 800 h in closed environment (100 %RH)

Name	BET surface area (m^2 g^{-1})	Total pore volume (cm^3 g^{-1})[a]	Micropores volume (cm^3 g^{-1})[c]
13X(b)-*ws*	724	0.35	0.27
13X(b)@Ca-*ws*	558	0.28	0.20
LiX(b)-*ws*	742	0.41	0.28
LiX(b)@Ca-*ws*	559	0.35	0.21

[a] Determined for P/P_0 = 0.99. [c] Determined using the t-plot N_2.

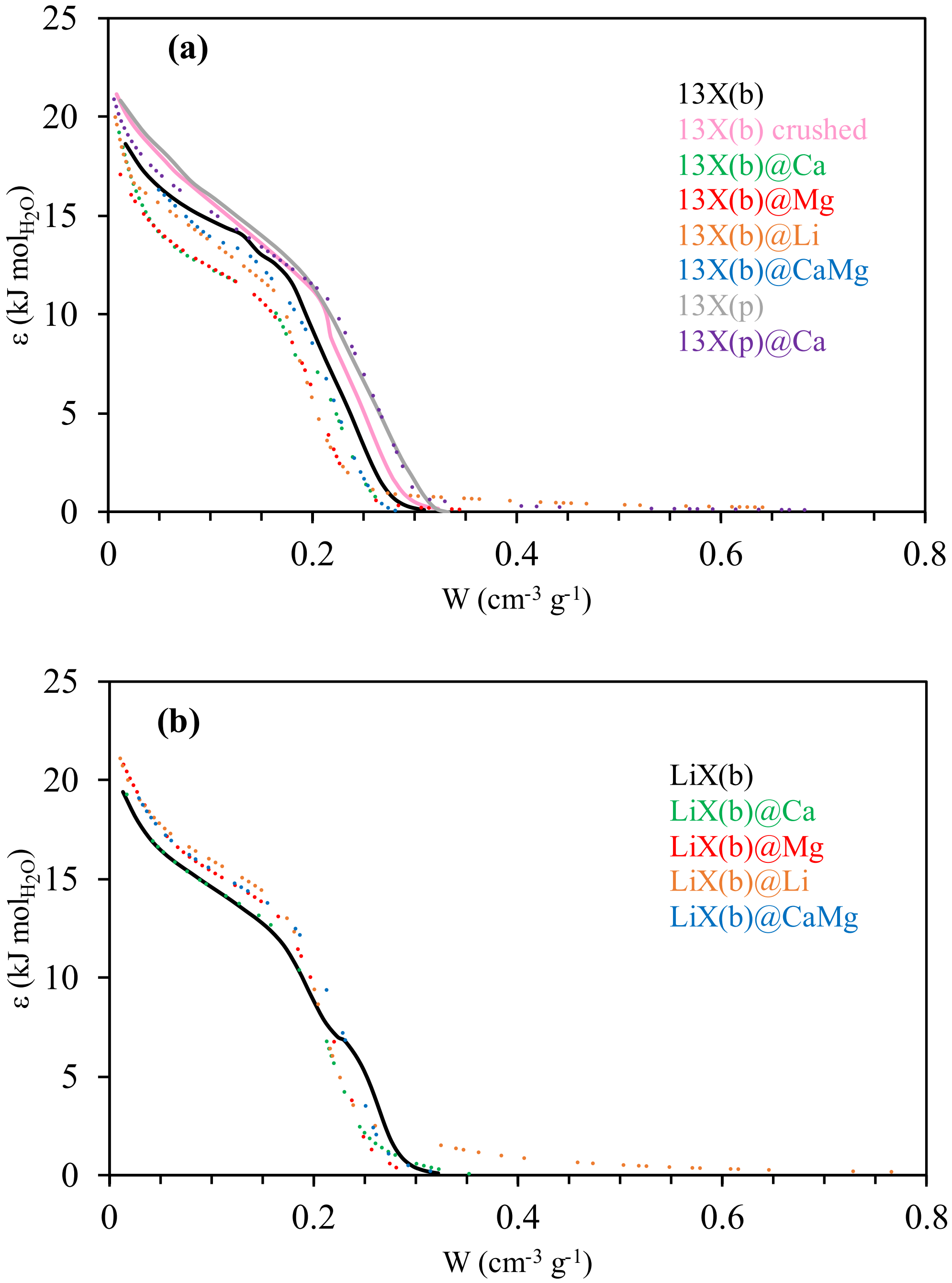

Figure S19. Evolution of the adsorption potential of water molecules in function of the water uptake of 13X (a), LiX(b) (b) and corresponding composites.

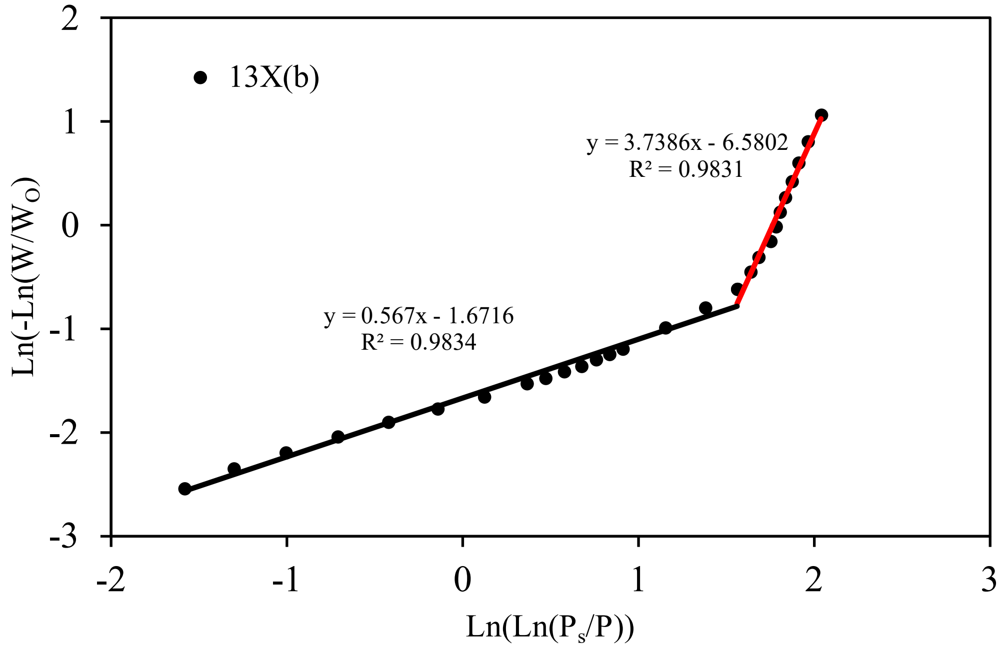

Figure S20. Linear transform of the Dubinin-Astakhov model of 13X(b).

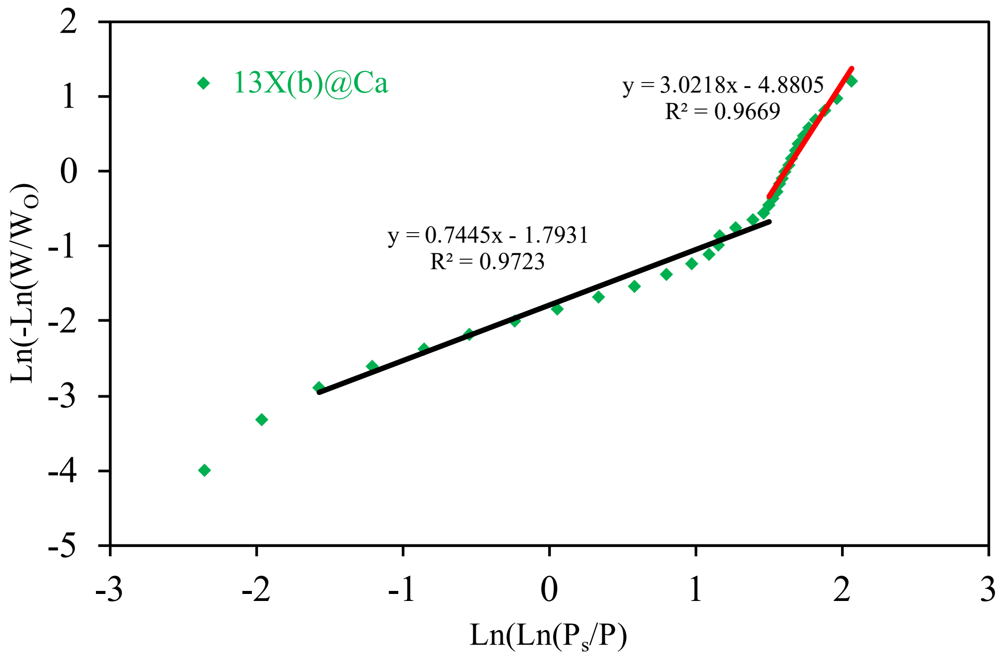

Figure S21. Linear transform of the Dubinin-Astakhov model of 13X(b)@Ca.

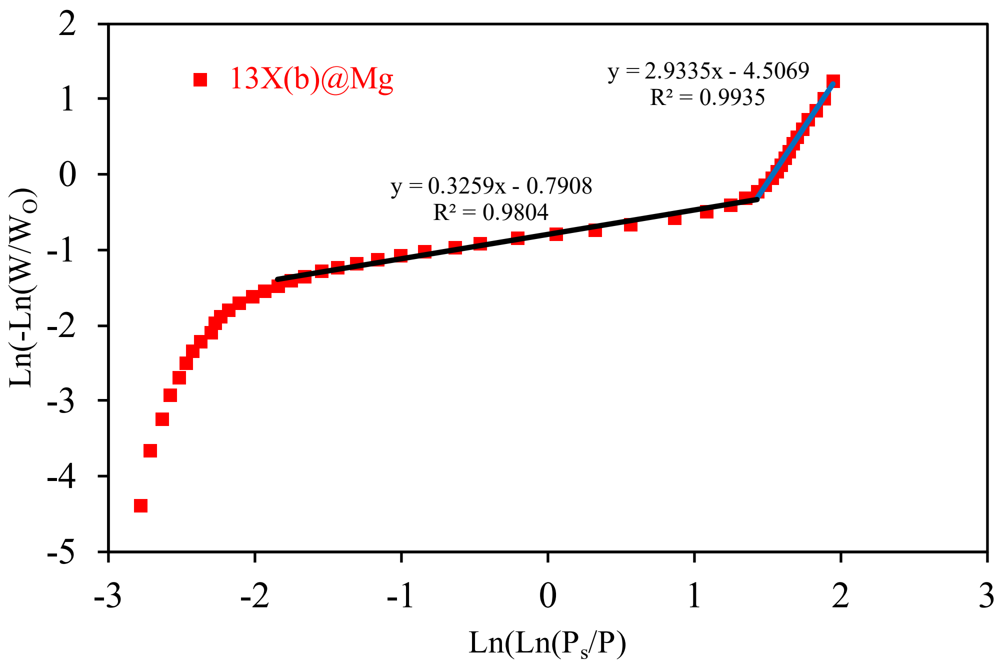

Figure S22. Linear transform of the Dubinin-Astakhov model of 13X(b)@Mg.

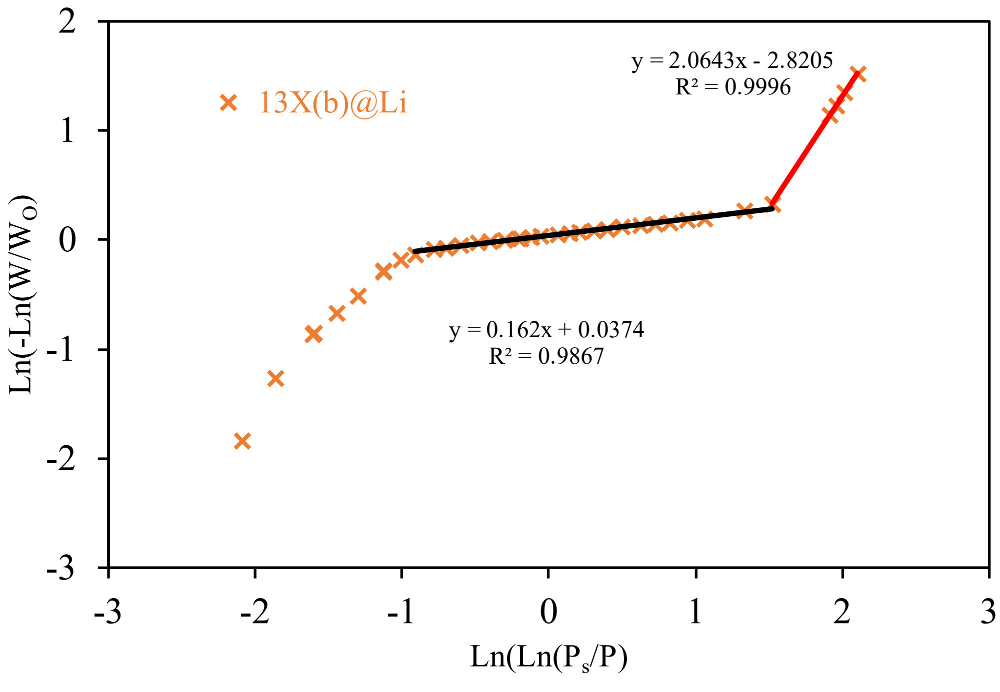

Figure S23. Linear transform of the Dubinin-Astakhov model of 13X(b)@Li.

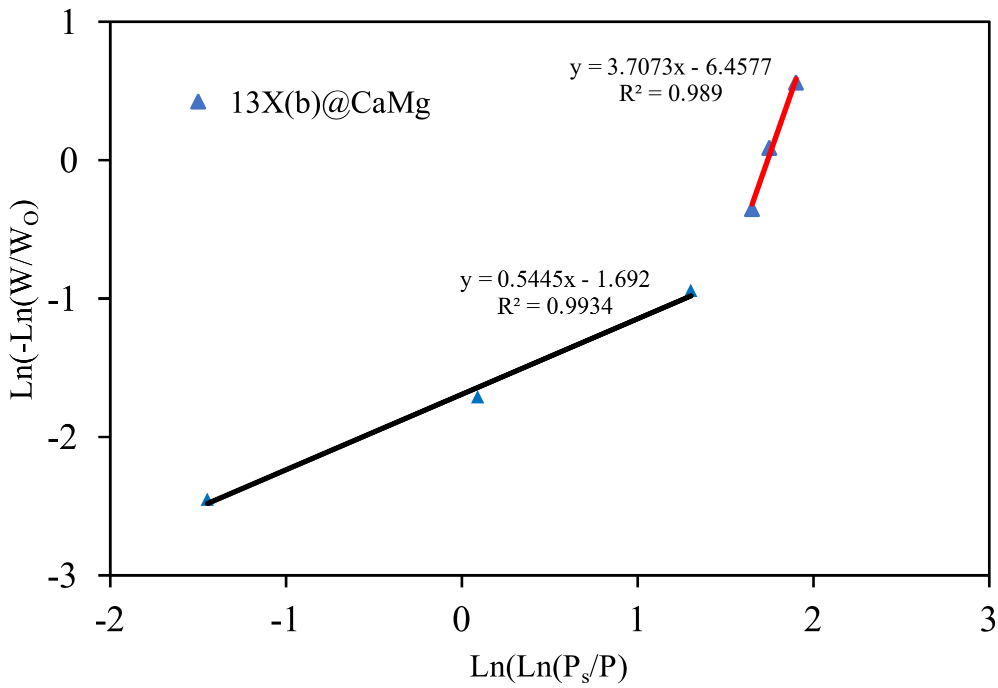

Figure S24. Linear transform of the Dubinin-Astakhov model of 13X(b)@CaMg.

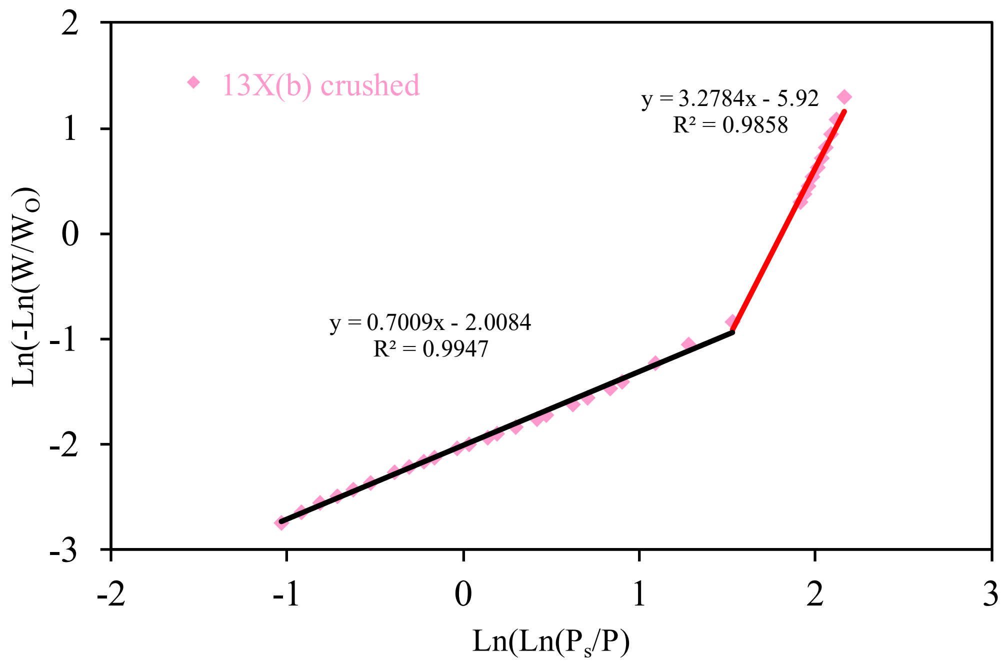

Figure S25. Linear transform of the Dubinin-Astakhov model of 13X(b) crushed.

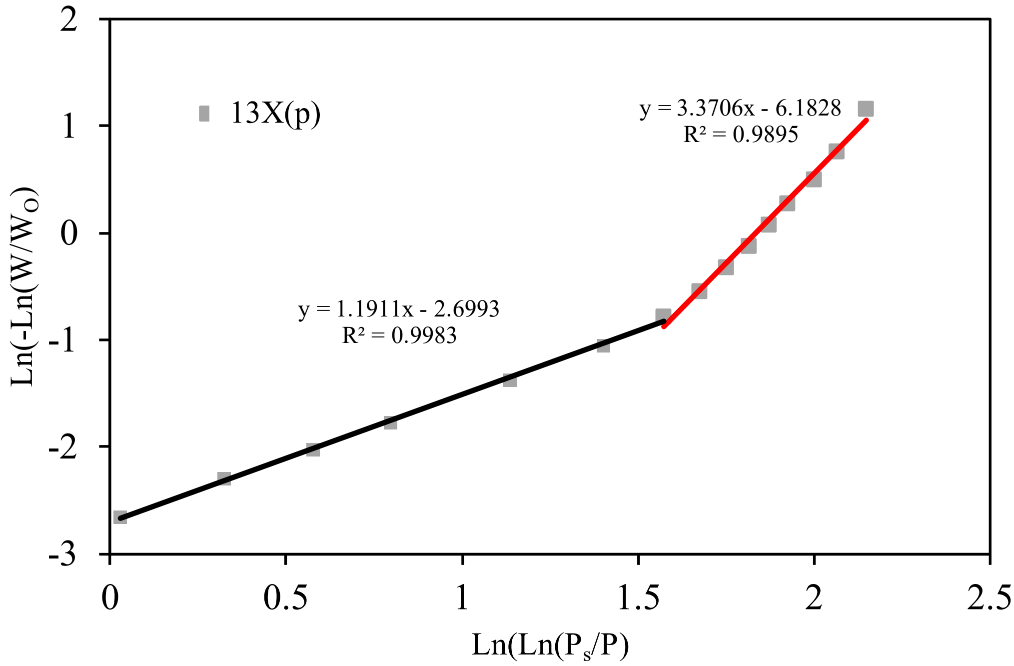

Figure S26. Linear transform of the Dubinin-Astakhov model of 13X(p).

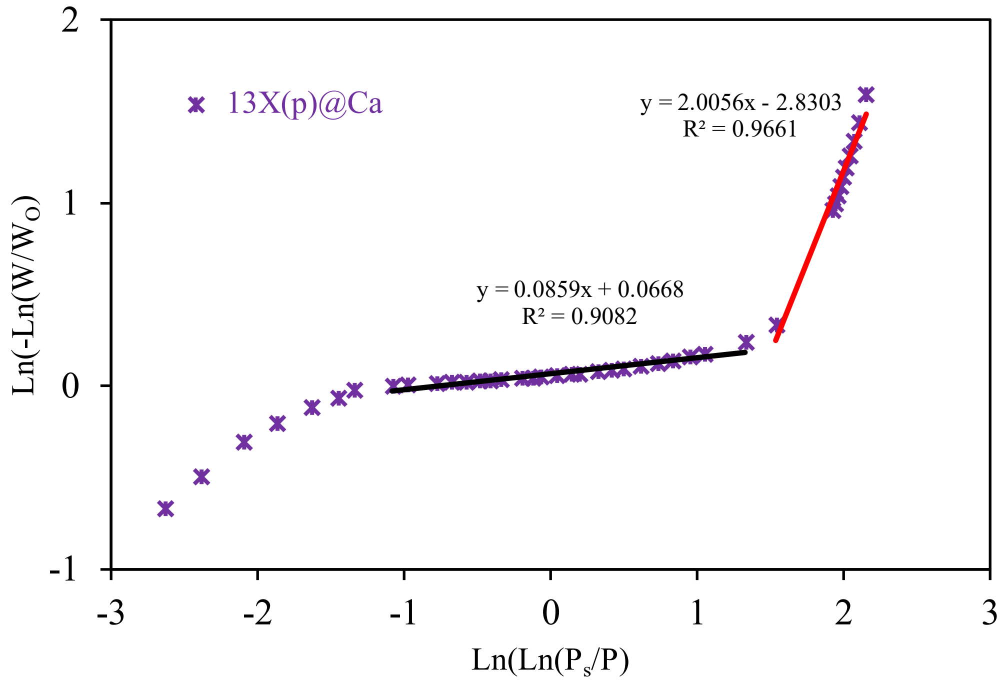

Figure S27. Linear transform of the Dubinin-Astakhov model of 13X(p)@Ca.

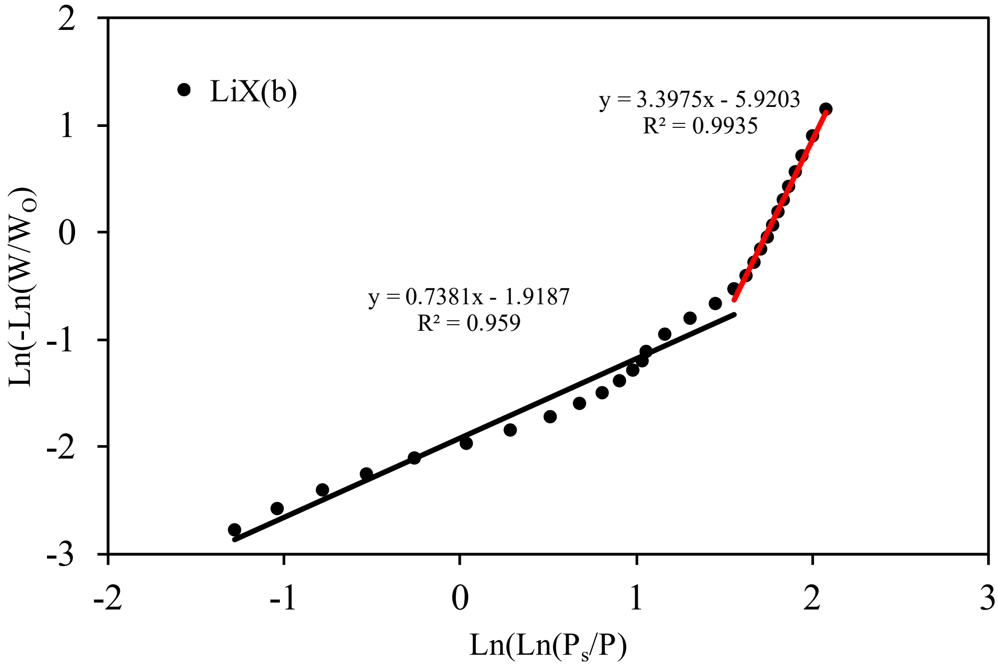

Figure S28. Linear transform of the Dubinin-Astakhov model of LiX(b).

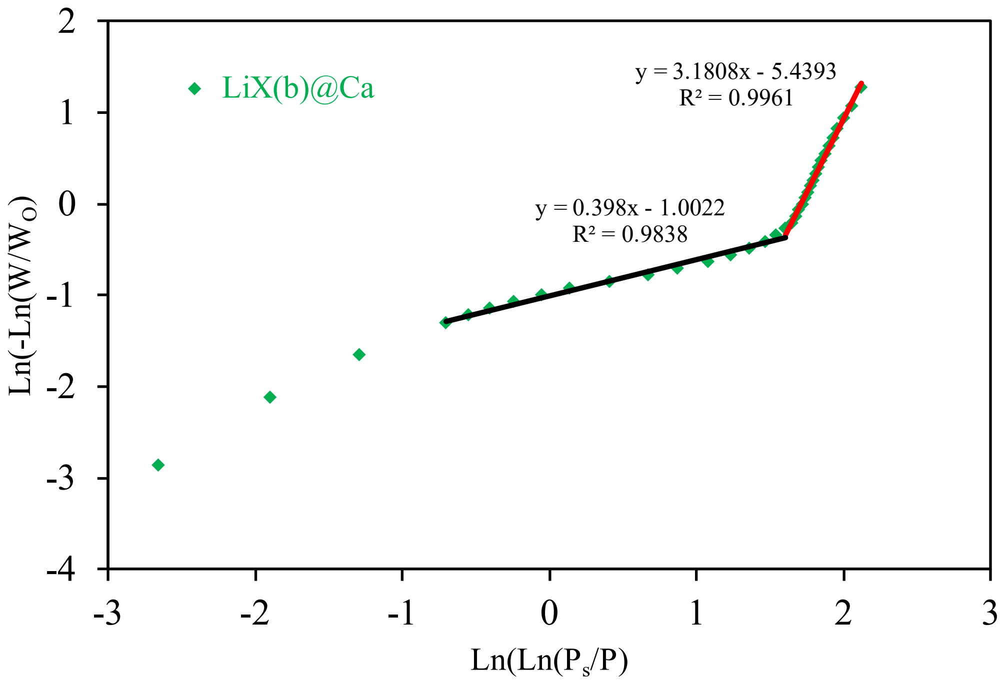

Figure S29. Linear transform of the Dubinin-Astakhov model of LiX(b)@Ca.

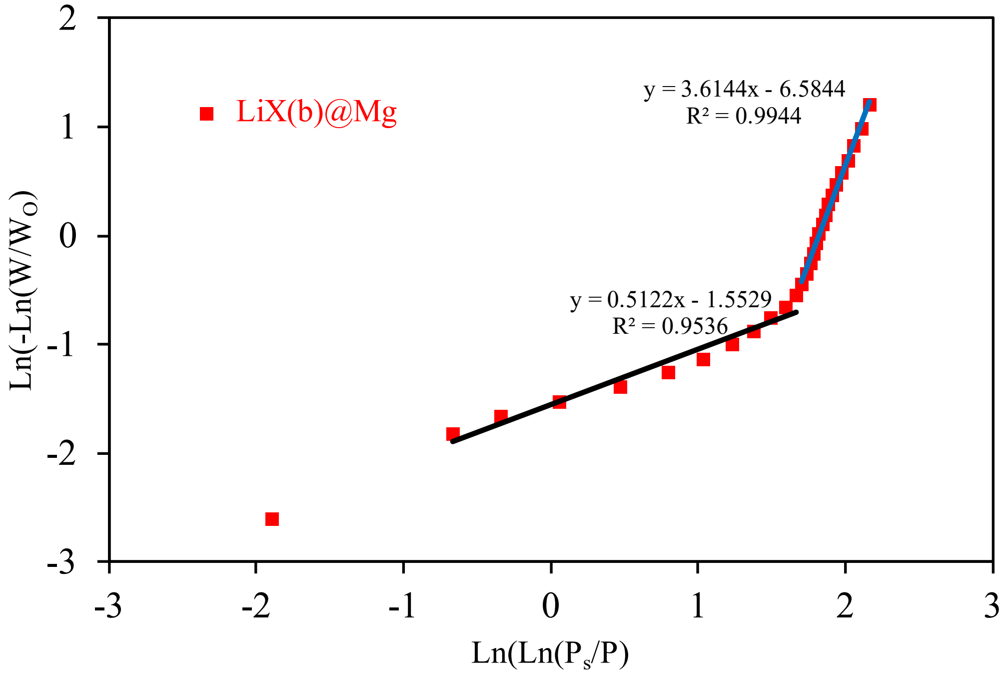

Figure S30. Linear transform of the Dubinin-Astakhov model of LiX(b)@Mg.

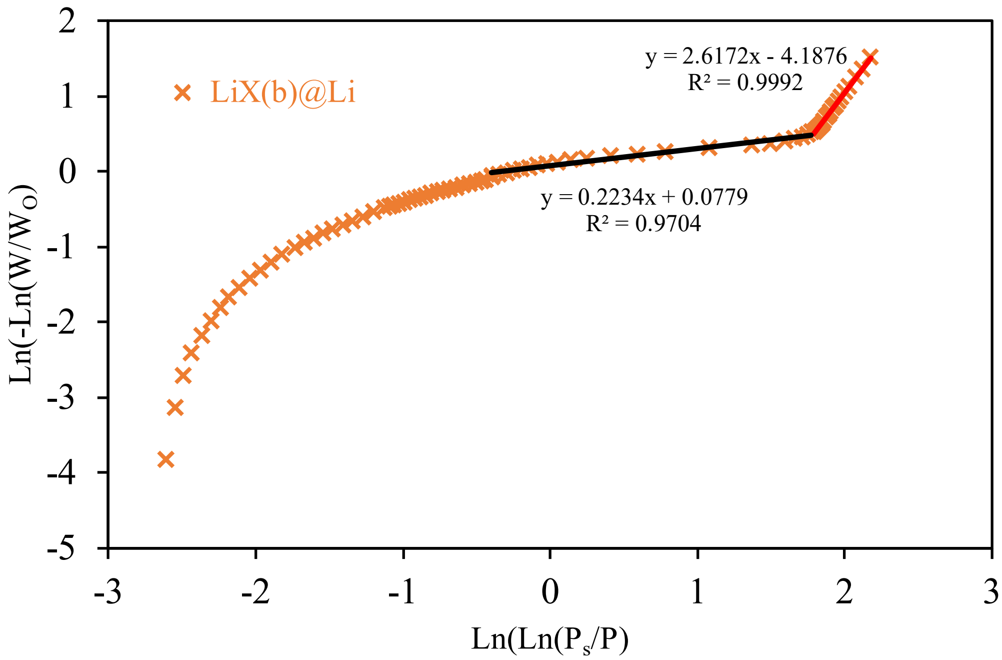

Figure S31. Linear transform of the Dubinin-Astakhov model of LiX(b)@Li.

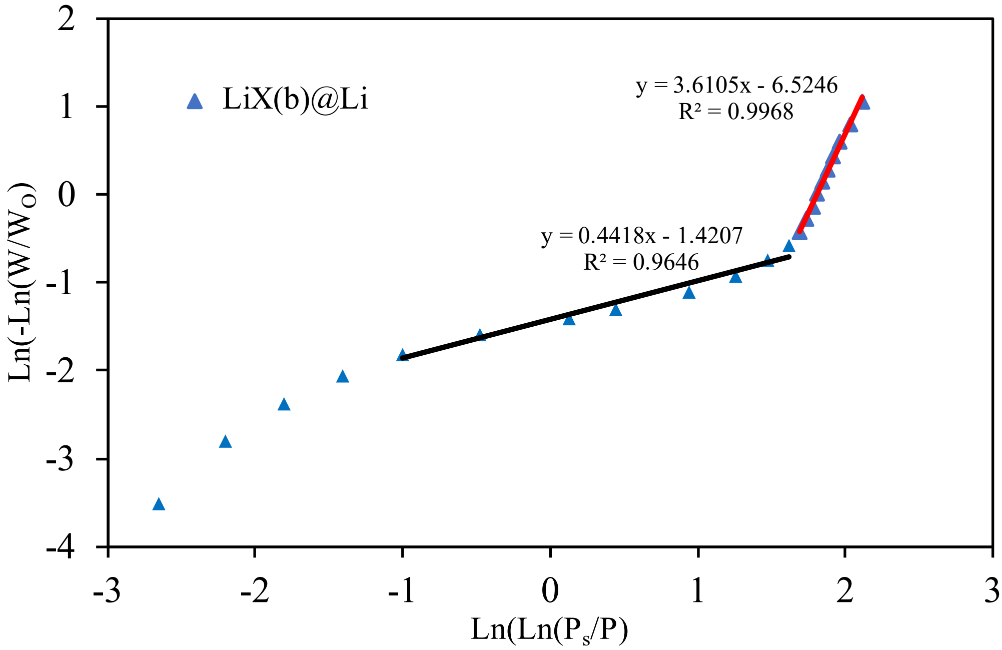

Figure S32. Linear transform of the Dubinin-Astakhov model of LiX(b)@CaMg.

Dubinin and Asktakhov model equations:

This model is described by Eq. (S1):

$$W' = W_0 exp\left(\frac{-\varepsilon}{E}\right)^n where E = \frac{\beta}{\sqrt{K}} \wedge \varepsilon = RTln\left(\frac{P_s}{P}\right) \quad \text{(S1)}$$

This equation can be transformed to a linear one by taking logarithms:

$$ln(W') = ln(W_0) - \left(\frac{RT}{E} ln\left(\frac{P_S}{P}\right)\right)^n$$

$$ln\left(-ln\left(\frac{W'}{W_0}\right)\right) = nln\left(\frac{RT}{E}\right) + nln\left(ln\left(\frac{P_s}{P}\right)\right)$$

In these equations, *K* represents the pore distribution constant, *β* the affinity coefficient of the sorptive, *Ps* the saturation pressure, *P* the partial pressure of water vapor, *W'* the amount of water sorbed, and *We* the maximal sorbed amount. The order of distribution *n* reflects the heterogeneity of the solid: *n* increases with the degree of homogeneity of the solid structure

Table S3. Parameters of the Dubinin-Astakhov adsorption model.

sample	θ[a]	n[b]	R^2
13X(b)	θ < 0.64	3.75	0.9831
	θ > 0.64	0.57	0.9834
13X(b)@Ca	θ < 0.63	3.02	0.9669
	θ > 0.63	0.74	0.9723
13X(b)@Mg	θ < 0.49	2.93	0.9935
	θ > 0.49	0.33	0.9804
13X(b)@Li	θ < 0.27	2.06	0.9996
	θ > 0.27	0.16	0.9867
13X(b)@CaMg	θ < 0.66	3.71	0.9890
	θ > 0.66	0.54	0.9934
13X(b) crushed	θ < 0.68	3.28	0.9858
	θ > 0.68	0.70	0.9947
13X(p)	θ < 0.64	3.37	0.9895
	θ > 0.64	1.19	0.9983
13X(p)@Ca	θ < 0.30	2.00	0.9661
	θ > 0.30	0.08	0.9082
LiX(b)	θ < 0.64	3.40	0.9935
	θ > 0.64	0.74	0.9590
LiX(b)@Ca	θ < 0.50	3.18	0.9961
	θ > 0.50	0.40	0.9838
LiX(b)@Mg	θ < 0.62	3.61	0.9944
	θ > 0.62	0.51	0.9536
LiX(b)@Li	θ < 0.18	2.62	0.9992
	θ > 0.18	0.22	0.9704
LiX(b)@CaMg	θ < 0.61	3.61	0.9968
	θ > 0.61	0.44	0.9646

[a] Filling factor determined at the intersection of the two regression lines.
[b] The parameter n corresponds to the slope of the regression lines.

References

[1] G. Whiting, D. Grondin, S. Benici, A. Auroux, Heats of water sorption studies on zeolite- $MgSO_4$ composites as potential thermochemical heat storage materials, Sol. Energy Mater. Sol. Cells 12 112-119 (2013). https://doi.org/10.1016/j.solmat.2013.01.020.

[2] A. Jabbari-Hichri, S. Bennici, A. Auroux, Effect of aluminium sulfate addition on the thermal storage performance of mesoporous SBA-15 and MCM-41 materials, Sol. Energy Mater. Sol. Cells 149 231-241 (2016). http://doi.org/10.1016/j.solmat.2016.01.033.

[3] J. Jänchen, D. Ackermann, E. Weiler, H. Stach, W. Brösicke, Calorimetric investigation on zeolites, $AlPO_4$'s and $CaCl_2$ impregnated attapulgite for thermochemical storage of heat, Thermochim. Acta 434 37-41. https://doi.org/10.1016/j.tca.2005.01.009.

[4] S.X. Xu, Lemington, R.Z. Wang, L.M. Wang, J. Zhu, A zeolite 13X/magnesium sulfate–water sorption thermal energy storage device for domestic heating, Energy Conver. Manag. 171 98-109 (2018). https://doi.org/10.1016/j.enconman.2018.05.077.

[5] Q. Wang, Y. Xie, B. Ding, G. Yu, F. Ye, C. Xu, structure and hydration state characterizations of $MgSO_4$-zeolite 13x composite materials for long-term thermochemical heat storage, Sol. Energy Mater. Sol. Cells 200 110047 (2019). https://doi.org/10.1016/j.solmat.2019.110047.

[6] A. Jabbari-Hichri, S. Bennici, A. Auroux, Enhancing the heat storage density of silica–alumina by addition of hygroscopic salts ($CaCl_2$, $Ba(OH)_2$, and $LiNO_3$), Sol. Energy Mater. Sol. Cells. 140 351–360 140 (2015). https://doi.org/10.1016/j.solmat.2015.04.032.

[7] A. Ristic, N. Zabukovec Logar, New composite water sorbents $CaCl_2$-PHTS for low-temperature sorption heat storage: determination of structural properties, 9 27 (2019). https://doi.org/10.3390/nano9010027.

[8] A. Permyakova, S. Wang, E. Courbon, F. Nouar, N. Heymans, P. D'ans, N. Barrier, P. Billemont, G. De Weireld, N. Steunou, M. Frère, C. Serre, Design of salt-metal organic framework composites for seasonal heat storage applications. J. Matter. Chem. A 5 12889 (2017). https://doi.org/10.1039/c7ta03069j.
[9] L. Silvester, Q. Touloumet, A. Kamaruddin, F. Chassagneux, G. Postole, A. Auroux, L. Bois, Influence of silica functionalization on water sorption and thermochemical heat storage of mesoporous SBA-15/CaCl2 composites, ACS Appl. Energy Mater. 4 5944-5956 (2021). https://doi.org/10.1021/acsaem.1c00786.